Aerodynamic performance of aircraft wings with stationary vertical lift propellers

Oliver Westcott *, Swathi Krishna, Robert Entwistle, Mario Ferraro

University of Southampton, Burgess Road, Southampton, SO16 7QF, Hampshire, UK

A B S T R A C T

Improvements in battery and motor technology are facilitating innovative aircraft configurations capable of vertical take-off and landing. Of these configurations, lift+cruise is popular for its inherent redundancy and the option to tailor separate propulsion systems for each flight regime. During cruise, the vertical flight propellers of a lift+cruise design are inactive and often exposed. Increasing the projected area of a body is understood to increase the drag, but the aerodynamic performance of an edgewise, stationary propeller and its influence on neighboring bodies is less clear. This study aimed to quantify the impact of two, tandem, edgewise and stationary propellers on the aerodynamic performance of a wing using wind tunnel measurements. The stationary position of the front and rear propellers were varied in 30° increments between 0-150°, at angles of attack between -4° and 10°. Results at Re = 4.3×10^5 showed the propellers and supporting systems had negligible influence on the lift. However, a drag increase of up to 30% was recorded when propeller positions were aligned perpendicular to the wing chord instead of parallel. Variations in the stationary position of the propeller altered the lift to drag ratio by up to 36% in a typical cruise configuration.

© 2023 The Author(s). Published by Elsevier Masson SAS. This is an open access article under the CC BY license (http://creativecommons.org/licenses/by/4.0/).

1. Introduction

The advent of electric Vertical Take-Off and Landing (VTOL) aircraft and the ever present demand for increased range and endurance, has led to a wide range of configurations for achieving efficient forward flight in combination with adequate vertical flight performance [1], [2]. The main types of wing-borne electric VTOL aircraft can be classified as lift+cruise, thrust vectoring, and aircraft tilting. Lift+cruise and thrust vectoring are the most commonly adopted, as the gap to conventional aircraft design is smaller and existing technology can often be repurposed. For the small Uncrewed Aerial Vehicles (UAVs) concerned within this research, the complexity of manufacturing a reliable variable-pitch rotor means most aircraft in the thrust vectoring class of VTOL UAV design still use a fixed-pitch propeller. By using the same fixed-pitch propeller for vertical and forward flight, the number of required propellers is often reduced [3]. However, the efficiency of a thrust vectoring design's propulsion system may be compromised as the propeller and motor are required to operate in the two distinctly different regimes of vertical and forward flight. For lift+cruise designs, the choices of propellers and motors for forward and vertical flight are

decoupled, and can be optimized for their individual regimes. In addition to the propulsive and drive train efficiencies that may be gained from the correct propeller and motor choices, lift+cruise designs also remove the necessity to carry and develop the complex and often heavy tilting mechanisms required for vectored thrust designs. A lift+cruise design will also benefit from a level of inherent redundancy due to the segregation of the vertical and forward flight systems. This added redundancy is very valuable when designing systems that require a high tolerance to failure, such as an aircraft.

The trade-off for having tailored propulsion systems and inbuilt redundancy is that lift+cruise designs have to carry the additional weight of the independent vertical flight propulsion systems for the remainder of the mission - this inevitably has a penalty in terms of range and endurance. Another drawback to consider in the use of lift+cruise designs, is the aerodynamic penalty contributed by the inactive and often exposed vertical flight propellers during the cruise portion of the mission. This aerodynamic penalty can be reduced by applying fairings and even mechanisms to retract the propellers into a more streamlined position [4]. However, these drag reduction methods also contribute additional mass, cost and, in the case of a retraction mechanism, additional complexity and potential reliability issues. An intermediary solution employed on most crewed electric VTOL aircraft and some large UAVs is to use the motor controller to align the propellers to a specific orien-


Nomenclature

α	Angle of incidence	°
$\bar{c}$	Mean geometric chord length	m
ϕ	Disc-wing loading factor	
θ	Stopped azimuthal propeller angle	°
AR	Aspect ratio	
b	Wingspan	m
c	Wing chord length	m
C_D	Drag coefficient	

C_L	Lift coefficient	
D_P	Propeller diameter	m
K_Q	Disc volume coefficient	
n	Number of propellers	
S	Wing area	m²
S_P	Single propeller area	m²
V_∞	Free-stream velocity	ms⁻¹
x_B	Propeller center to center distance	m
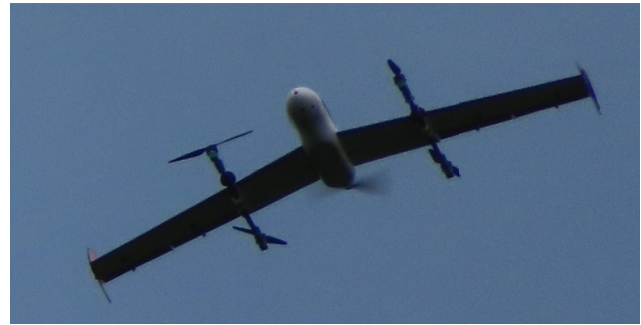
(a) Example 1

(b) Example 2

Fig. 1. Examples of inactive propeller positions for a lift+cruise design in forward flight. Images from flight testing of the VALERIE (Vertical Ascent and Landing aircraft for Experimental Research, Investigation and Exploration) aircraft in April 2022.

tation, usually parallel to the slipstream. However, this feature is not commonly available on commercial motor designs at the small UAV scale, which is where this research will focus. What is more common across the majority of electric motor designs is the option to use the motor controller to apply a braking force to the motor when it is not in use. This braking force has no feedback and therefore the propeller may come to rest at any point in its rotation when the aerodynamic forces on the blades are exceeded by the braking force - this condition is described as a stopped propeller. Studies previously conducted have analyzed the influence of the active vertical lift propellers on each other and the impact of the inflow conditions on the propeller performance [5], [6]. However, the impact of a tandem pair of stopped, edgewise propellers on the aerodynamic performance of a lift+cruise wing does not appear to have been investigated in much granularity. Bacchini et al. [7] investigated the viability of retracting the vertical flight systems into the aircraft to reduce drag in cruise. Their results showed that this did offer an improvement in aerodynamic performance. During their experiments, they also measured the drag on the aircraft with vertical flight propellers aligned in perpendicular and parallel directions to the flow. The four stopped propellers all had the same alignment, which is unlikely in actual flight conditions without an additional mechanism to perform the alignment. The stopped propeller positions occurring in the forward flight of a lift+cruise design that only uses motor controller braking to arrest the rotation of the vertical flight propellers may not always be this consistent (Fig. 1). To the best of the authors' knowledge, no other studies were found that systematically confirmed or quantified the fundamental effects of adding each of the systems required to convert a conventional wing design to one capable of lift+cruise.

This paper aims to build on the work presented in [7], by carrying out a systematic investigation of the effect of different stopped propeller angles on the aerodynamic performance of a lift+cruise design's wing. Through the novel experiments carried out in this study, we aim to:

1. Quantify the relative contribution of individual components in a VTOL subsystem to the overall lift and drag of the model in comparison to a conventional wing.
2. Quantify the effect of varying stopped propeller angles on the aerodynamic performance of the model.
3. Propose a simplified approximation for the change in the drag on a propeller with the variation of its stopped propeller angle.

The above contributions may then be used by future designers to build simple models during the initial design phases of lift+cruise vehicles and to explore the trade-offs between applying drag reduction devices such a fairings and retraction mechanisms or leaving the VTOL system exposed.

2. Methodology

A wind tunnel model was designed to investigate the influence of the stopped propeller angle on the aerodynamic performance of a lift+cruise wing. The model was a scaled semi-span of an existing lift+cruise wing belonging to a previous University of Southampton design, VALERIE (Fig. 1). Although, the methodology developed below could also be applicable to similar designs in the lift+cruise class. The azimuthal angle relative to the wing chord-line at which the blade comes to rest under the braking force of the motor drive, is referred to here as the stopped angle of the propeller, θ, (Fig. 2b). The stopped angle of the propeller is defined relative to the leading edge of the blade, with a positive angle being defined as a rotation in the direction opposite to that necessary for generating lift.
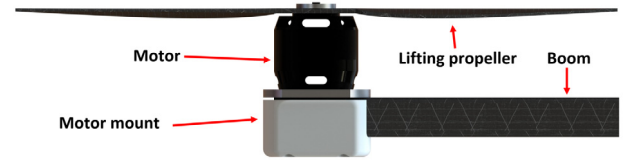
2.1. VALERIE

VALERIE (Vertical Ascent and Landing aircraft for Experimental Research, Investigation and Exploration) is a lift+cruise, delta-wing configuration using four lifting propellers, and was designed at the University of Southampton for remote sensing missions [8].
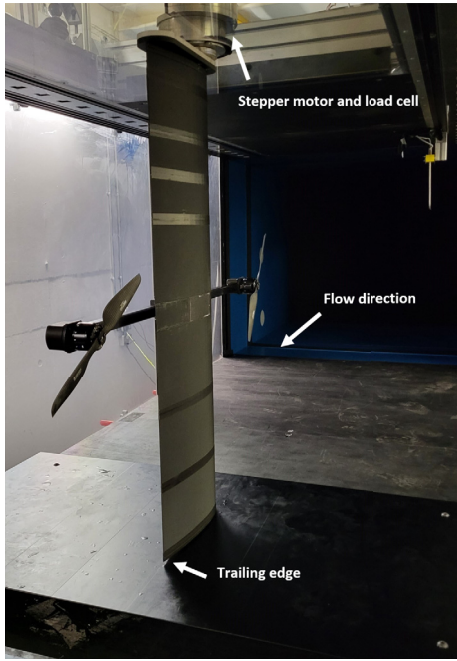
(a) Wind tunnel model mounted in the Boundary Layer Wind Tunnel at the University of Southampton.
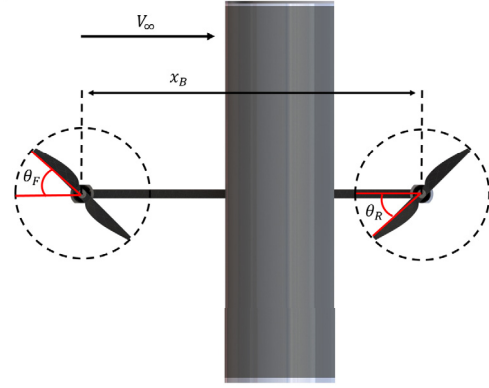
(b) Reference geometry for the stopped azimuthal front θ_F, and rear θ_R, propeller angles and propeller separation distance x_B, of an aircraft wing in free-stream velocity V_∞.

(c) The end of one boom showing the various components of the VTOL subsystem.

Fig. 2. Wind tunnel model setup, reference dimensions and VTOL subsystem description.

VALERIE is an established and capable aircraft which displays favorable control characteristics in vertical and forward flight. The scaling methodology outlined below aims to generate a wind tunnel model with similar control characteristics by maintaining the relative scale of the vertical flight propellers to the wing surface and their separation from each other.

2.2. Non-dimensional scaling

Two non-dimensional scaling parameters were derived to generate the wind tunnel geometry using the reference dimensions of VALERIE as the inputs. The disc volume coefficient K_Q and disc-wing loading factor ϕ, are non-dimensional terms obtained during the derivation of a pitching moment equation for a lift+cruise design. Here n is the number of propellers, S is the main wing area and S_P the area of a single propeller disc. The propeller disc centers are separated by a distance x_B, and the main wing chord length is denoted as c.

$$\phi = \frac{n S_P}{S} \tag{1}$$
$$K_Q = \phi \frac{x_B}{c} \tag{2}$$

2.3. Testing facility

The wind tunnel tests were conducted in the Boundary Layer Wind Tunnel (Fig. 2a), located at the University of Southampton. The wind tunnel has a working section of 1.0 m x 1.2 m x 12 m (height x width x length), is temperature controlled and can operate at velocities up to 40 ms^{-1}. The tunnel was set to maintain a constant ratio of wing Reynolds number to kinematic viscosity via a feedback loop to account for variations in tunnel operating conditions. The angle of attack of the model is controlled by a stepper motor in the upper surface of the tunnel working section. The forces and torques acting on the model are measured by an ATI Delta IP65 SI-660-60 sensor, located in series with the stepper motor.

2.4. Tunnel model geometry

The semi-span of the model was chosen as 0.9 m, with a splitter plate added coincident with the tip to reduce the presence of three-dimensional wing effects. A rectangular planform with a NACA2415 profile was selected. The sweep from VALERIE was not matched in the scaled geometry to ensure the model was as simple and generalized as possible. In this way, the fundamental behavior of the propeller and wing interaction could first be understood, without observing effects caused by more complex planform designs. The aspect ratio AR, of the VALERIE wing was conserved in the wind tunnel model, allowing the scaled chord length c, of the tunnel model to be calculated. The propeller diameter for the tunnel model was selected by attempting to conserve the disc-wing loading factor (ϕ) from VALERIE. It was not possible to match ϕ exactly, as commercial propellers are only manufactured in discrete diameters. Therefore, the propeller diameter for the tunnel model was rounded to the nearest inch. This allowed a commercial propeller of the same design as VALERIE to be purchased and paired to an appropriate motor model (Fig. 2c). There are notably a range of different motors that are compatible with a single propeller diameter and their differences can often result in a range of efficiencies and power outputs from the motor-propeller system. From initial research, the available motor options all appear to be regular cylinders. Previous work investigating the drag on cylindrical bodies [9], could allow the drag measurements made here to be adapted to approximate the effect of different motor sizes. With ϕ determined for the tunnel model, conservation of the disc volume coefficient (K_Q) is used to define the distance between propellers x_B (Table 1). The model was constructed from a series of 3D printed Poly-Lactic Acid (PLA) sections mounted on steel spars. A square carbon-fiber box section, termed the 'boom' was used to transfer the forces from the VTOL motors to the wing structure. The stopped azimuthal angle of the propeller to the boom center line (θ), which is parallel to the wing chord-line (Fig. 2b), was varied and then locked by fastening the motor casing to its base with a grub screw.
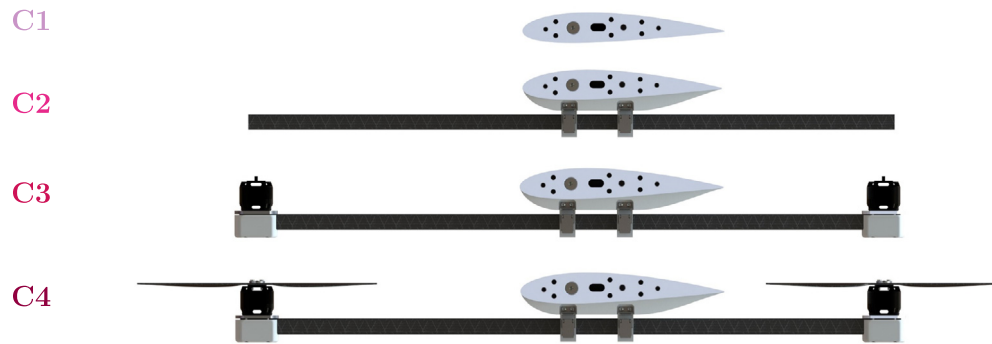
Fig. 3. Wind tunnel model configurations, where C1 is the clean wing, C2 is the wing with the boom and its attachment to the wing, C3 is the wing with the boom and its attachment to the wing, the motors and their mounts and C4 is the wing with the boom and its attachment to the wing, the motors and their mounts and the lifting propellers.

Table 1
Characteristics of VALERIE and the scaled wind tunnel model.

Parameter	VALERIE	Wind tunnel model
Wing span (b):	2.5 m	1.8 m
Wing area (S):	0.90 m²	0.47 m²
Aspect ratio (AR):	6.94	6.94
Propeller diameter (D_P):	0.43 m (17")	0.31 m (12")
Propellers per semi-span ($n/2$):	2	2
Disc area (S_P):	0.15 m²	0.07 m²
Disc center to center (x_B):	1.09 m	0.81 m
Free-stream velocity (V_∞):	22 ms⁻¹	25 ms⁻¹
Mean geometric chord ($\bar{c}$):	0.36 m	0.26 m
Wing Reynolds number (Re):	5.6×10^5	4.3×10^5
Disc-wing loading factor (ϕ):	0.65	0.63
Disk volume coefficient (K_Q):	1.95	1.95
Propeller model:	T-motor P17x5.8	T-motor P12x4
Motor model:	T-motor V505 260 kV	T-motor U5 400 kV

2.5. Experimental procedure

For a conventional aircraft wing to be capable of VTOL, the addition of a 'VTOL subsystem' is required. The VTOL subsystem includes the boom and its attachment to the wing, the motors and their mounts, and the lifting propellers (note that the power electronics are neglected from this term as being out of scope for this experiment). An understanding of the relative contribution of each component in the VTOL subsystem to the aerodynamic performance of the model was developed by incrementally adding components to the previously clean wing. The impact of the stopped propeller angle on the aerodynamic performance of the completed model was then investigated. The configurations tested are shown in Fig. 3 as:

1. The clean wing (C1).
2. The wing with the boom and its attachment to the wing (C2).
3. The wing with the boom and its attachment to the wing, the motors and their mounts (C3).
4. The wing with the boom and its attachment to the wing, the motors and their mounts and the lifting propellers (C4).

It is assumed that any results collected at stopped propeller angles in the range 180-360° are equivalent to those in the range 0-180°, as the propeller is symmetric after a 180° rotation about its center. By the same logic, a measurement at 180° is equivalent to one at 0°. The tunnel model is a starboard wing with the front propeller set to rotate counter-clockwise and the rear propeller clockwise. This distinction is made because it is necessary to have motors and propellers arranged to generate zero net torque on the vehicle. Data was collected at each combination of front and rear stopped propeller angles in the space 0-150° with 30° increments. This produced 36 stopped propeller angle combina-

tions. Each set of 36 combinations was then measured in the angle of attack range -4° to 10° with 2° increments. The feedback loop for the tunnel was set to maintain a ratio of the wing Reynolds number to kinematic viscosity equivalent to a free-stream velocity of 25 ms⁻¹. This provided the best compromise between not exceeding the root bending moment of the load cell and matching the wing Reynolds number of VALERIE in cruise. An initial set of experiments were conducted to determine the required sampling duration for the main experiment. For a free-stream velocity of 25 ms⁻¹ and a wing chord length of 0.26 m, the convection time-scale of the model is on the order of 0.01 seconds. The sampling duration was selected as 100 seconds at 10 kHz to allow approximately 10,000 convection cycles to elapse per sample duration. This provided a reduced data set of an equivalent number of statistically independent points for analysis. The 99% confidence interval was calculated for the reduced data set, showing the error on the mean of the force data was lower than the resolution of the force sensor provided in the data sheet of the manufacturer. The uncertainty (U) of the lift and drag coefficients (C_L and C_D) was determined using the sensitivity coefficients of the equations for C_L and C_D, and the resolutions of the measurement apparatus. The maximum absolute relative percentage errors on the lift and drag coefficients found during all measurements were $|U_{CL}/C_L| = 1.7\%$ and $|U_{CD}/C_D| = 10.9\%$ respectively.

3. Results

The hypothesis entering this experiment was that the addition of the VTOL subsystem to the clean wing would increase the drag across all angles of attack. The increase in drag was expected to be caused by an increase in the wetted area of the model and the introduction of bluff bodies like the motor casings and exposed structural members. The minimum drag propeller configuration was expected to occur when both propellers were aligned parallel to the chord-line of the wing, $\theta = 0°$ in reference to Fig. 2b. The maximum drag condition was expected when both propellers were perpendicular to the chord-line of the wing, $\theta = 90°$. The basis for this hypothesis was that the projected propeller area is minimized and maximized respectively for each scenario. The drag induced by the stopped propeller was predicted to vary cyclically with the stopped angle of the propeller and to take the form of a function with a maximum value at $\theta = 90°$ and a minimum at $\theta = 0°$. Total drag was expected to follow the trend of the main wing variation with angle of attack. However, it was likely that flow interactions between the propellers and the wing might influence the results. The effect on the lift measured was expected to vary similarly to the drag response, but with smaller relative magnitude as the forces generated by the wing would likely dominate the variations introduced by the VTOL subsystem. It was conceived that the flow
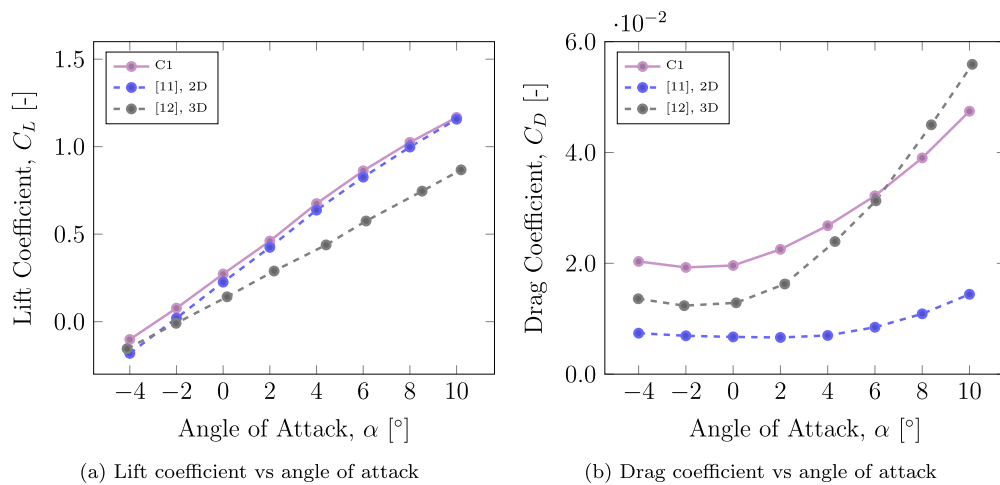
(a) Lift coefficient vs angle of attack

(b) Drag coefficient vs angle of attack

Fig. 4. Lift and drag coefficient comparison for the clean wing configuration (C1) with data from literature. The C1 configuration is tested at Re = 4.3×10^5, NACA 2415 sectional data [11] at Re = 3.0×10^6 and NACA 2415 finite wing data [12] at Re = 3.0×10^6, AR = 6.

exiting the front propeller might impinge on the main wing, and therefore the stopped angle of the front propeller would be most influential.

3.1. Clean wing performance

The tunnel model was initially configured in the clean wing configuration as C1. The C1 lift coefficient is plotted against data from literature in Fig. 4a. The lift coefficients show a linear variation with angle of attack, as expected for a NACA 4-series profile before the stall region. The coincidence of the root profile to the tunnel wall and the splitter plate at the tip, both act to minimize the flow of air from the high to low pressure side of C1 wing's surface. By minimizing the movement of air between the upper and lower surfaces, the wing is less affected by the downwash generated and the sectional lift curve slope of the profile is more closely preserved [10]. This preservation of the lift curve slope appears to be occurring for C1, with a gradient of the lift curve of 5.3 rad^{-1}, comparing closely to the 5.5 rad^{-1} of the sectional data in [11]. The finite wing data of [12] displays the suggested reduction of the lift-curve slope at 4.1 rad^{-1}, as a result of the generated downwash.

Fig. 4b compares the drag polar of C1 to a finite wing from literature; also plotted is the sectional drag coefficient of the NACA2415 aerofoil used in the C1 and finite wing cases. Comparing C1 to the finite wing presented in the work of Jacobs [12], the trend of the curves between -4° and 0° appears similar, with both seeming to share the same minimum drag angle of attack around -2°. However the magnitude of the polars is offset, with the drag on the finite wing of [12] being on average 0.007 or 34% smaller than for C1 between -4° and 0°. This difference in drag is attributed to the difference in Reynolds number and the relatively rough surface finish of the 3D printed sections of C1. In contrast, the models in [12] had smoother surfaces made from duralumin [13]. The surface roughness of the model can increase the drag as a result of an increase in the skin friction drag coefficient, where a smooth and polished finish is preferential for drag reduction [14]. At angles of attack greater than 0°, the drag on the finite wing of [12] increases much more rapidly with angle of attack than C1. This suggests that the splitter plate mounted at the tip of C1 is effectively reducing the strength of the wing tip vortices that would form and are likely present in the case of the finite wing. Wing tip vortices produce induced drag on a wing and are a function of the square of the lift coefficient, which is approximately the trend observed in the drag polar of the finite wing from literature.

3.2. General impact of VTOL subsystems on aerodynamic performance

After obtaining a baseline for the aerodynamic performance of a clean wing with C1, the components of the VTOL subsystem were incrementally added in configurations C2, C3 and C4. This piece-wise addition of the components necessary for VTOL flight allowed the identification of the major contributors to the change in aerodynamic performance and how their contribution changed with angle of attack. In addition, the influence of the stopped azimuthal position of the front and rear propeller on the lift and drag of the C4 configuration is investigated.

The addition of the components making up the VTOL subsystem are shown to have minor influence on the lift production capabilities of the model in any configuration across the angle of attack range measured (Fig. 5a). Additionally, variations in stopped propeller angles in the C4 configuration were found to have only a very small influence on the lift coefficient of the model. This suggests that flow exiting the stopped front propeller was not significantly disturbing the flow across the downstream wing, which might have promoted flow separation or other phenomena resulting in a sudden loss of lift from the wing. Furthermore, the variation in stopped propeller position does not appear to offer any significant lift enhancement, even when orientated perpendicular to the wing chord-line, where the largest projected area is expected from each stopped propeller.

As each component of the VTOL subsystem is introduced, the wetted area increases generating a mixture of profile and induced drag (Fig. 5b). Contrary to our hypothesis the drag introduced is not always proportional to the wetted area increase. For the motor's comparatively small addition of wetted area, a relatively large increase in drag is observed; likely due to the bluff body geometry of the motor casing. The trend of each configuration's drag polar follows the underlying shape of C1 at positive angles of attack, but at larger relative magnitudes. The addition of VTOL components appears to increase the drag at negative angles of attack almost symmetrically to positive angles of attack. C1 on the other hand, has a much smaller increase in drag at negative angles of attack. The addition of the VTOL subsystem appears to shift the minimum drag location towards 0°, instead of −2° in the case of the C1. However, the change in drag measured between these two configurations is within the measurement error for the experiment so cannot be conclusively determined. For the C2 configuration, the ends of the boom were left uncapped. The uncapped ends might have allowed a form of pipe flow, increasing friction drag due to flow through the boom's interior, producing the almost symmet-
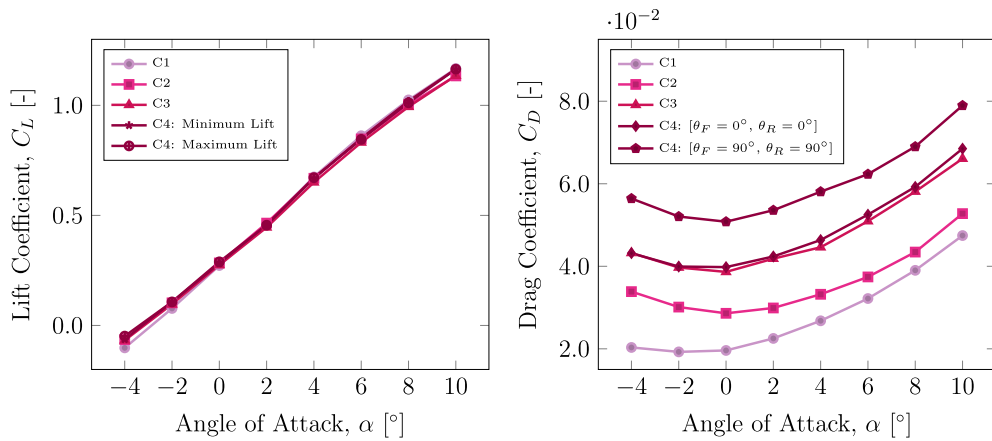
(a) Lift coefficient vs angle of attack. The maximum lift series shows the highest lift coefficient recorded for the C4 configuration out of the 36 stopped propeller combinations, the minimum lift series shows the lowest lift coefficients out of the 36 stopped propeller combinations.

(b) Drag coefficient vs angle of attack. Where θ_F = front propeller azimuthal angle and θ_R = rear propeller azimuthal angle.

Fig. 5. Lift and drag coefficient comparison for the wind tunnel model in various configurations, where C1 (Clean wing), C2 (Wing and Boom), C3 (Wing, Boom and Motors) and C4 (Wing, Boom, Motors and Propellers).

ric increase in drag for positive and negative angles of attack. This effect would not be observed in configurations C3 and C4 as the ends of the boom are capped by the motor mounts. To test the hypothesized minimum and maximum drag propeller configurations, C4 was configured with stopped azimuthal angles for the front (θ_F) and rear (θ_R) propellers of [$\theta_F = 0°$, $\theta_R = 0°$] and [$\theta_F = 90°$, $\theta_R = 90°$]. The expected minimum drag propeller configuration at [$\theta_F = 0°$, $\theta_R = 0°$] is shown to have a negligible effect on the drag of the model at small and negative angles of attack when compared to the drag measured without propellers installed (C3). When the stopped angle of the propellers is set to the expected maximum drag configuration, [$\theta_F = 90°$, $\theta_R = 90°$], a drag increase of up to 30% is observed in comparison to the propellers aligned parallel to the wing chord-line.

At each angle of attack in the range $\alpha = -4°$ to 10°, configuration C4 was tested with each of the 36 stopped propeller combinations as described in Section 2.5. The stopped propeller angles of the front and rear propeller that produced the local maximum and minimum drag coefficient at each angle of attack are marked with a (○) and (△) respectively (Fig. 6). For negative angles of attack, the local minimum drag occurs at [$\theta_F = 0°$, $\theta_R = 0°$]. When the angle of attack is 0° and above, the local minimum drag shifts to [$\theta_F = 150°$, $\theta_R = 150°$] for the remaining angles of attack. The azimuthal propeller angle combinations for the local minima are close to the expected positions at [$\theta_F = 0°$, $\theta_R = 0°$], based on an argument of minimizing projected propeller area producing the lowest drag. However, $\theta_F = 150°$ appears to consistently generate the lowest drag at positive angles of attack. The twist of the propeller blade along its span may be leveraging a more favorable flow path over the blade at $\theta_F = 150°$, resulting in a lower drag than at $\theta = 0°$ for positive angles of attack. This is despite the projected propeller area not being at a minimum. Additionally, the flow exiting the front propeller may be impinging on the wing and rear propeller more favorably. The local maximum drag locations occur for azimuthal propeller angles in the range [$\theta_F = 60 - 90°$, $\theta_R = 60 - 90°$], which is generally as would be expected based on an argument of maximizing propeller projected area producing the largest drag. The alternating positions for the azimuthal angles producing maximum local drag might be explained by the propeller blade twist or that the flow from the front propeller is interacting with the wing differently. In our future work, we suggest investigating this hypothesis using flow visualization. At negative angles of attack and large positive angles of attack, the

stopped angle of the propellers has a larger, more widespread influence on the drag of the model. This effect can be observed in the subplots of Fig. 6 as the regions of higher drag occupy larger proportions of the plot, instead of being arranged in more concentrated areas around the azimuthal angles with maximum projected propeller area. At large angles of attack, the effect of a larger α will also increase the projected area of the propeller beyond just the effects caused by variations in the azimuthal angle. Larger α could also result in flow separation over the blades leading to stall and the regions of higher drag. Some symmetry in Fig. 6 is observed across the plane intersecting [$\theta_F = 0°$, $\theta_R = 0°$] and [$\theta_F = 180°$, $\theta_R = 180°$] for angles of attack -4° to 4°. Complete symmetry was not predicted as the wing and front propeller were expected to influence the flow over the rear propeller. Above 4°, the approximate symmetry begins to deteriorate. The regions of highest drag become more rectangular, with the long axis of the rectangle being orientated to variations in the front propeller angle. This suggests that the stopped angle of the rear propeller begins to have a larger relative effect on the drag of the model at higher angles of attack. The shift in the relative importance of the stopped propeller angles suggests that the flow over the front propeller may already be separated and hence changes in its stopped angle have a smaller impact on the drag. At larger angles of attack, the rear propeller is likely still experiencing an amount of downwash from the main wing. The downwash produced by the main wing reduces the local angle of attack experienced by the rear propeller, meaning flow over the rear propeller blade may stay attached for longer.

Adding the VTOL subsystem to the C1 configuration has been shown to cause a significant increase in drag for a small change in the lift produced (Fig. 5). The resulting effect is a reduction in the maximum lift to drag ratio, on the order of 33% for C4 compared to C1 (Fig. 7). The local maximum and minimum lift to drag ratios for each angle of attack are plotted in Fig. 7 and labeled with the stopped propeller angles at which they occur as (θ_F, θ_R). The variations in the stopped propeller angle have a larger relative influence on the drag on the model compared to the lift (Fig. 5). For this reason, the stopped propeller angles producing the highest and lowest local lift to drag ratios are heavily influenced by the stopped angles for the highest and lowest drag configurations. The angle of attack for the model to achieve the highest lift to drag ratio is also increased when compared to C1. Therefore, the velocity at which the maximum lift to drag occurs may now be different
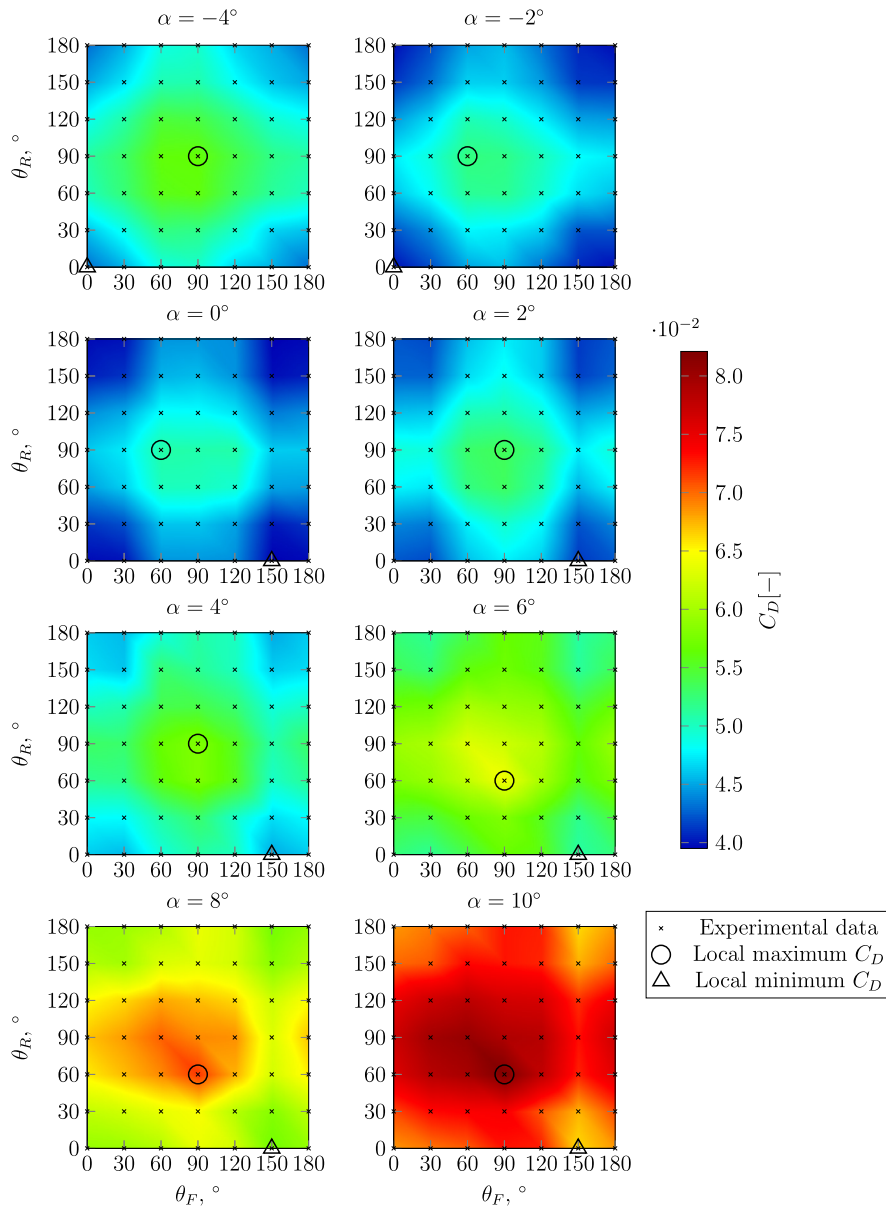
Fig. 6. C4 drag coefficient for varying front and rear stopped propeller angles at increasing angles of attack, α, where θ_F and θ_R are the azimuthal stopped angle of the front and rear propeller respectively. The local maximum value of C_D for the 36 stopped propeller angles at each angle of attack is marked by a ($\circ$) and the local minimum value by a ($\triangle$). (For interpretation of the colors in the figure(s), the reader is referred to the web version of this article.)

for a lift+cruise design using the same wing planform as a conventional aircraft.

3.3. Impact of stopped propeller angle on aerodynamic performance

A case study for cruise at an angle of attack, $\alpha = 2°$ is presented below, with α chosen in reference to the cruising attitude of VALERIE. After transitioning to the wing-borne cruise segment of the flight, the vertical flight propellers of a lift+cruise design will usually remain inactive. As the cruise segment is typically the longest part of a flight, understanding the aerodynamic penalty of the stopped propeller angle in the cruise configuration will likely translate to the largest improvement in range and endurance for the vehicle.

3.3.1. Impact on drag
Fig. 8a shows the change in the drag coefficient of the model for a series of stopped rear propeller angles with fixed front pro-

peller angles, at a model angle of attack of 2°. The curves in Fig. 8a cluster into two groups, with $\theta_F = 90° + / - 30°$ consistently producing the largest drag coefficients and $\theta_F = 0° + / - 30°$ producing the lowest drag coefficients. The data for the $\theta_F = 90°$ curve is fitted with a modified cosine function $f(\theta_R)$ which approximates the drag of an isolated stopped propeller - this uses the simplifying assumption that drag is a function of the frontal area of a propeller, which in turn is a function of the cosine of the stopped angle. The trend of the curve for each stopped front propeller angle is approximated reasonably well by the modified cosine function. The best match between the cosine approximation and the experimental data is unsurprisingly close to the local maxima and minima used to fit the curve. The largest differences between the cosine approximation and the experimental data were 2.4% at $\theta_R = 60°$ and 2.7% at $\theta_R = 120°$. This deviation is expected as the propeller blades are not symmetric about 90° of rotation. The close match between the isolated propeller approximation and the experimental data for the rear propeller suggests that the stopped azimuthal
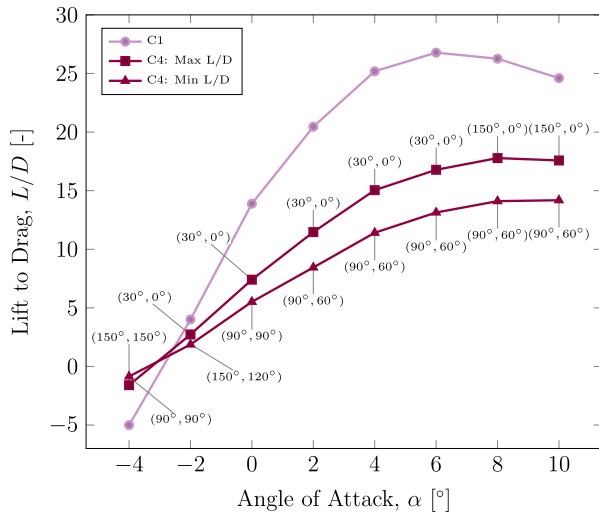
Fig. 7. Lift to drag ratio vs angle of attack. C1 = Clean Wing, C4 = Wing, Boom, Motors and Propellers, Max L/D = Maximum Lift to Drag Propeller Configuration and Min L/D = Minimum Lift to Drag Propeller Configuration. Each point is labeled with (θ_F, θ_R) representing the stopped propeller configuration at which the local maximum or minimum lift to drag ratio was recorded for that angle of attack.

angle of the rear propeller only appears to affect the drag on the rear propeller as it is downstream of the other components.

Fig. 8b shows the change in the drag coefficient of the model as the front stopped propeller angle is varied for fixed rear propeller angles at a model angle of attack of 2°. The same stopped propeller angles producing the maximum and minimum drag are observed for the stopped rear propeller as were described in Fig. 8a, although their order of influence on the drag is slightly altered. The same modified cosine function is fitted to the curve $\theta_R = 90°$, but now with less similarity to the experimental data observed. Both the cosine function and experimental data show a maximum drag at $\theta_F = 90°$. However, the cosine function predicts the minimum drag to occur at $\theta_F = 0°$, as would correspond to the minimum projected area. Conversely, the experimental data shows two inflection points at $\theta_F = 30°$ and $\theta_F = 150°$, with $\theta_F = 150°$ consistently being the minimum drag configuration. The minimum drag configuration for the stopped front propeller does not coincide with the minimum projected area, in contradiction to the cosine approximation. It is likely the blade twist of the front propeller is leveraging a drag reduction due to a more favorable flow path over the blades or that the flow over the wing and rear propeller causes less drag at this stopped front propeller angle. This will be confirmed in future flow visualization studies.

3.3.2. Impact on lift

As noted in Section 3.2, variation in the stopped propeller angle tends to have a relatively small effect on the lift coefficient of the C4 configuration. The variation in the lift coefficient of C4 caused by different stopped front and rear propeller angles is approximately 12% at $\alpha = 2°$ (Fig. 9). Whereas the same stopped propeller configurations resulted in approximately 23% variation in the drag coefficient of C4 at the same angle of attack (Fig. 8). If the propellers are simplified to an approximation of a straight wing, changing the stopped angle could approximate changing the sweep angle of the wing. Previous work has shown that increasing the sweep angle reduces the achievable lift coefficient by approximately the cosine of the quarter-chord sweep angle [15]. If a stopped propeller angle of 90° is taken as a wing with zero sweep angle (perpendicular to oncoming flow), then the response of the lift coefficient to changing stopped propeller angles would be expected to be a minimum at 0°, increasing to a maximum at 90° and then returning to a minimum at 180°. For the fixed

rear propeller angles shown in Fig. 9b, as the stopped front angle is increased from $\theta_F = 0 - 60°$, the lift coefficient increases as the advancing blade is effectively swept less. At $\theta_F = 90°$, the advancing and retreating blade are now equally exposed to the flow, and the lift generated is less than at $\theta_F = 60°$. A net positive lift was still expected as the camber and twist of the advancing blade is likely more effective at generating lift than the rearward side of the retreating blade is at producing down force. After $\theta_F = 90°$, the lift produced is relatively constant with stopped front propeller angle, decreasing back to a minimum as θ_F approaches 180°. There is the possibility that flow exiting the front stopped propeller is also influencing the lift produced by the wing and rear propeller; although it isn't possible to confirm this interaction without some form of flow visualization. At this angle of attack, Fig. 9b shows that any increase in the stopped front propeller angle increases the lift coefficient of the model.

Fig. 9a shows the change in the lift coefficient of C4 as the rear stopped propeller angle is varied for fixed front propeller angles at a model angle of attack of 2°. It appears that for most stopped front propeller angles, any increase above $\theta_R = 0°$ will result in a reduction in the lift coefficient at this angle of attack. The reduction in C4's lift coefficient for the rear propeller angle range $\theta_R = 0 - 90°$ at most angles of θ_F, suggests that the rear propeller may be experiencing a local negative angle of attack due to the downwash from the wing. In comparison to the trends for each fixed rear propeller angle shown in Fig. 9b, the curves for fixed front propeller angles shown in Fig. 9a are more dispersed. This dispersion suggests the front propeller angle has more influence on the lift coefficient of C4 than the rear propeller at this angle of attack. This could be because the position of the front stopped propeller partially dictates the flow condition over the wing and rear propeller.

3.3.3. Impact on the lift to drag ratio

Fig. 10 shows the change in the lift to drag ratio (L/D) of the C4 configuration as the front and rear stopped propeller angles are varied at a model angle of attack of 2°. The difference between stopped propeller positions producing the local minimum and local maximum L/D locations for this cruise attitude could result in a 36% variation in the lift to drag ratio. With L/D being analogous to the aerodynamic efficiency of the configuration, controlling the stopped azimuthal angle of the front and rear propellers has the potential to significantly improve the range and endurance of a lift+cruise design in the absence of fairings or retraction mechanisms. Controlling the stopped position of the front and rear propellers will require an additional system. However, this type of propeller position control is now being offered by at least one commercial motor manufacturer at the UAV scale - with the system included in a very similar or identical motor footprint. Therefore, the mass and drag penalty of switching out an existing motor should not adversely affect the performance of a lift+cruise design.

4. Conclusions and future work

This study aimed to understand the impact of the incremental addition of VTOL subsystems to a previously clean wing configuration, a comparison relevant to the design of a lift+cruise wing. Driven by observations of an existing aircraft in flight, a generalized scaled model of the wing and VTOL subsystems was built to systematically investigate the effect of varying the stopped positions of two lifting propellers on the aerodynamic performance of a lift+cruise wing. Force measurements were performed on a model wing in the wind tunnel, with different configurations of the VTOL subsystem installed. The quantitative data obtained through these experiments highlights the relative importance of
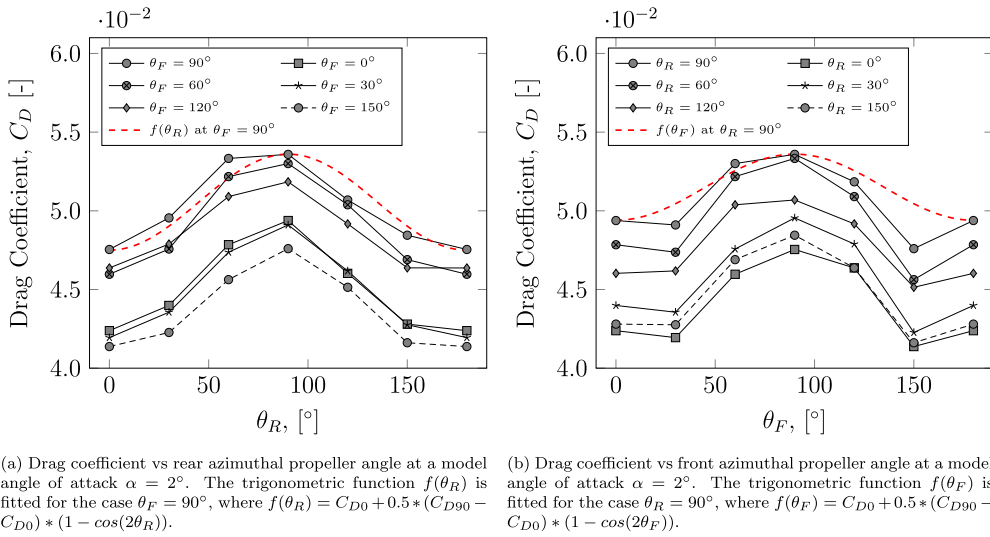
(a) Drag coefficient vs rear azimuthal propeller angle at a model angle of attack $\alpha = 2°$. The trigonometric function $f(\theta_R)$ is fitted for the case $\theta_F = 90°$, where $f(\theta_R) = C_{D0} + 0.5 * (C_{D90} - C_{D0}) * (1 - cos(2\theta_R))$.

(b) Drag coefficient vs front azimuthal propeller angle at a model angle of attack $\alpha = 2°$. The trigonometric function $f(\theta_F)$ is fitted for the case $\theta_R = 90°$, where $f(\theta_F) = C_{D0} + 0.5 * (C_{D90} - C_{D0}) * (1 - cos(2\theta_F))$.

Fig. 8. Drag coefficient comparison for varying front (θ_F) and rear (θ_R) stopped azimuthal propeller angles for the C4 configuration at an angle of attack $\alpha = 2°$. Here C_{D0} is the drag coefficient at $\theta = 0°$ and C_{D90} is the drag coefficient at $\theta = 90°$.

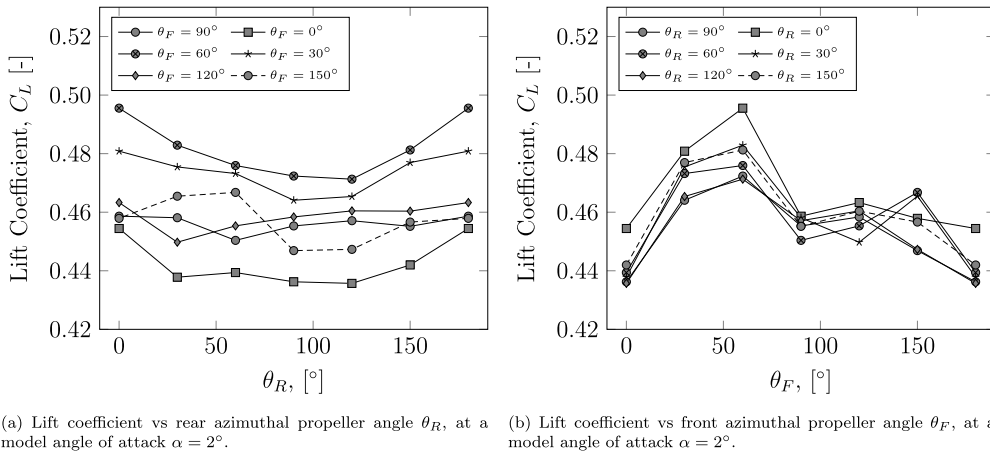(a) Lift coefficient vs rear azimuthal propeller angle θ_R, at a model angle of attack $\alpha = 2°$.

(b) Lift coefficient vs front azimuthal propeller angle θ_F, at a model angle of attack $\alpha = 2°$.

Fig. 9. Lift coefficient comparison for varying front (θ_F) and rear (θ_R) stopped azimuthal propeller angles for the C4 model at an angle of attack $\alpha = 2°$.
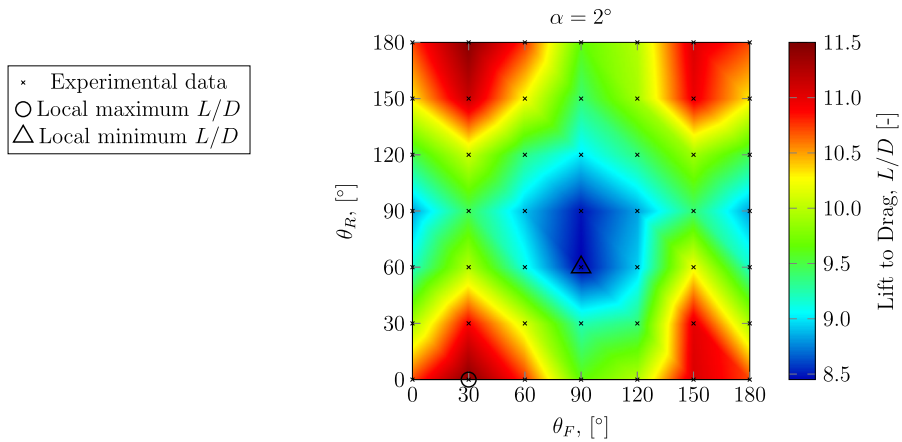

Fig. 10. Lift to drag ratio (L/D) for varying front (θ_F), and rear (θ_R), propeller angles for the C4 model at an angle of attack $\alpha = 2°$. The local maximum value of L/D is marked by a (○) and the local minimum value by a (△).

each component in the subsystem to the configuration's aerodynamic performance. Our findings through this experiment have led to the following conclusions:

- The addition of the VTOL subsystem has minimal relative effect on the lift produced by the lift+cruise design's wing in comparison to the clean wing. No significant change in the lift

coefficient was observed when varying the stopped azimuthal angle of the propellers.

- The addition of the VTOL subsystem increases the drag on the model considerably when compared to the clean wing. With both propellers aligned parallel to chord-line of the wing, the drag is very similar to the configuration without lifting propellers. Up to a 30% decrease in drag is observed when the propellers are parallel to the wing chord-line as compared to when both propellers are aligned perpendicularly.
- The maximum lift to drag ratio achievable with the VTOL subsystem installed is approximately 33% lower than maximum of the clean wing.
- At a typical cruise attitude, the stopped azimuthal angle of the front and rear propeller could result in a 36% variation in the lift to drag ratio of the model.
- For known drag values at the parallel and perpendicular azimuthal propeller positions, the variation in drag on the rear propeller for intermediate propeller angles can be approximated as a simple cosine function.

The benefits in terms of redundancy and potential propulsive and drive train efficiencies offered by lift+cruise designs will likely ensure that they remain an attractive option for future VTOL aircraft designs. However, the potential degradation in aerodynamic performance that might result from not controlling the stopped position of the vertical lift propellers has been shown to be significant, warranting special consideration in the early stages of the design process. The relative importance of each component commonly necessary to convert a conventional aircraft wing to a lift+cruise design has also been highlighted. This breakdown will allow future designers to effectively weigh-up the addition of fairings to streamline key pieces of the subsystem - e.g. the VTOL motors which contribute a significant amount of drag relative to their added mass and wetted area.

In future work we will investigate different propeller geometries with the aim of developing a propeller drag model based only on propeller geometry and a reference drag coefficient. By incorporating information about the wing geometry and its position in relation to the propellers, a generalized drag model based on the geometry alone may be possible. This development would accelerate the initial design process by reducing the need for additional physical testing. Developing a better understanding of the changes in aerodynamic performance as the geometry of the model is altered would also be important. By changing the separation between the propeller discs and their vertical separation from the chord-line of the wing and each other, it is possible some further improvements in aerodynamic performance could be achieved. Exploring changes in the position of the propellers relative to each other and the wing's surface may also offer valuable information about the noise generated by different configurations when the propellers are active. The use of a flow visualization technique such as Particle Image Velocimetry (PIV), could also be used to confirm some of the interactions conjectured in our findings.

Declaration of competing interest

The authors declare that they have no known competing financial interests or personal relationships that could have appeared to influence the work reported in this paper.

Data availability

Data will be made available on request.

References

[1] D.F. Finger, C. Braun, C. Bil, A review of configuration design for distributed propulsion transitioning vtol aircraft, in: Asia-Pacific International Symposium on Aerospace Technology-APISAT, 2017, pp. 3–5.

[2] A.S. Saeed, A.B. Younes, C. Cai, G. Cai, A survey of hybrid unmanned aerial vehicles, Prog. Aerosp. Sci. 98 (2018) 91–105, https://doi.org/10.1016/j.paerosci.2018.03.007, https://www.sciencedirect.com/science/article/pii/S0376042117302233.

[3] G.J. Ducard, M. Allenspach, Review of designs and flight control techniques of hybrid and convertible vtol uavs, Aerosp. Sci. Technol. 118 (2021) 107035, https://doi.org/10.1016/j.ast.2021.107035, https://www.sciencedirect.com/science/article/pii/S1270963821005459.

[4] P. Stahl, C. Rößler, M. Hornung, Benefit analysis and system design considerations for drag reduction of inactive hover rotors on electric fixed-wing vtol vehicles, in: 2018 Aviation Technology, Integration, and Operations Conference, 2018, p. 4150, https://arc.aiaa.org/doi/pdf/10.2514/6.2018-4150, https://arc.aiaa.org/doi/abs/10.2514/6.2018-4150.

[5] T.C.A. Stokkermans, D. Usai, T. Sinnige, L.L.M. Veldhuis, Aerodynamic interaction effects between propellers in typical evtol vehicle configurations, J. Aircr. 58 (4) (2021) 815–833, https://doi.org/10.2514/1.C035814.

[6] K. Pobikrowska, T. Goetzendorf-Grabowski, Wind tunnel tests of hovering propellers in the transition state of quad-plane, Bull. Pol. Acad. Sci., Tech. Sci. 69 (6) (2021) e138821, https://doi.org/10.24425/bpasts.2021.138821, http://www.journals.pan.pl/Content/120737/PDF/Z_23_02417_Bpast.No.69(6)_OK.pdf.

[7] A. Bacchini, E. Cestino, B. Van Magill, D. Verstraete, Impact of lift propeller drag on the performance of evtol lift+cruise aircraft, Aerosp. Sci. Technol. 109 (2021) 106429, https://doi.org/10.1016/j.ast.2020.106429, https://www.sciencedirect.com/science/article/pii/S1270963820311111.

[8] C. Boyd, O. Westcott, M. Ferraro, M.A. Erbil, R. Entwistle, Cascade open aircraft project: University of Southampton vtol drone development, in: AIAA Scitech 2021 Forum, 2021, https://arc.aiaa.org/doi/pdf/10.2514/6.2021-1929, https://arc.aiaa.org/doi/abs/10.2514/6.2021-1929.

[9] C.F. Heddleson, D.L. Brown, R.T. Cliffe, Summary of drag coefficients of various shaped cylinders, Tech. Rep., General Electric CO Cincinnati OH, 1957, https://doi.org/10.21236/ada388540.

[10] E. Houghton, P. Carpenter, S.H. Collicott, D.T. Valentine, Wing theory, Chapter 7, in: E. Houghton, P. Carpenter, S.H. Collicott, D.T. Valentine (Eds.), Aerodynamics for Engineering Students, seventh edition, Butterworth-Heinemann, 2017, pp. 449–523, https://www.sciencedirect.com/science/article/pii/B9780081001943000079.

[11] I.H. Abbott, A.E. Von Doenhoff, J. Stivers Louis, Summary of airfoil data, National Advisory Committee for Aeronautics, 1945, p. 137.

[12] E. Jacobs, K. Ward, R. Pinkerton, The characteristics of 78 related airfoil sections from tests in the variable-density wind tunnel, Report no. 460, National Advisory Committee for Aeronautics, 1933, p. 14.

[13] I.H. Abbott, E.N. Jacobs, The naca variable-density wind tunnel, National Advisory Committee for Aeronautics, 1933, p. 311.

[14] S. Gudmundsson, Chapter 15 - aircraft drag analysis, in: S. Gudmundsson (Ed.), General Aviation Aircraft Design, Butterworth-Heinemann, Boston, 2014, pp. 661–760, https://www.sciencedirect.com/science/article/pii/B9780123973085000155.

[15] S. Gudmundsson, The anatomy of the wing, Chapter 9, in: S. Gudmundsson (Ed.), General Aviation Aircraft Design, Butterworth-Heinemann, Boston, 2014, pp. 299–399, https://www.sciencedirect.com/science/article/pii/B978012397308500009X.